Minimum Torque Ripple Control for Brushless Doubly-Fed Induction Generator-DC System Under Power Winding Open-Phase Fault

Yi Liu, *Senior Member*, *IEEE*, Yizheng Zhang, Maoxin Zhang, Wei Xu, *Fellow*, *IEEE*, Shiyi Shao, *Senior Member*, *IEEE*, and Youguang Guo, *Senior Member*, *IEEE*

***Abstract* – In order to cope with the severe torque ripple caused by the open-phase fault of the power winding (PW) in the brushless doubly-fed induction generator-dc (BDFIG-DC) system, a novel minimum torque ripple control method is proposed in this article. The proposed method does not rely on additional external hardware devices and can minimize the torque ripple in the faulty system, thereby reducing damage to the machine bearings. Firstly, this article analyzes the harmonic components of the torque caused by PW open-phase fault in details, and derives the simplified torque expression. Secondly, by regulating the 3rd and 5th harmonic currents of PW, a minimum torque ripple control method is proposed. To obtain the real-time reference values of PW 3rd and 5th harmonic currents, the Newton's gradient descent method is adopted. Finally, the effectiveness of the proposed method is proven by comprehensive experimental results on a 5-kVA BDFIG-DC system platform.**

***Index Terms* - Brushless doubly-fed induction generator-dc (BDFIG-DC) system, open-phase fault, minimum torque ripple control, Newton's gradient descent method.**

This work was supported in part by the Guangdong Basic and Applied Basic Research Foundation under Grant 2023A1515012025, Shenzhen Fundamental Research Project (General Program) under Grant JCYJ20230807143701003, and National Natural Science Foundation of China under Grant 52277050. (*Corresponding author: Yizheng Zhang.*)

Yi Liu is with the State Key Laboratory of Advanced Electromagnetic Technology, School of Electrical and Electronic Engineering, Huazhong University of Science and Technology, Wuhan 430074, China, and also with the Research Institute of Huazhong University of Science and Technology in Shenzhen, Shenzhen 518057, China (e-mail: liuyi82@hust.edu.cn).

Yizheng Zhang and Maoxin Zhang are with the State Key Laboratory of Advanced Electromagnetic Technology, School of Electrical and Electronic Engineering, Huazhong University of Science and Technology, Wuhan 430074, China (e-mails: yzzhang18@hust.edu.cn; maoxin23@hust.edu.cn).

Wei Xu is with the Institute of Electrical Engineering, Chinese Academy of Sciences, Beijing 430074, China, and also with the Research Institute of Huazhong University of Science and Technology in Shenzhen, Shenzhen 518057, China (e-mail: weixu@mail.iee.ac.cn).

Shiyi Shao is with the CSSC Silent Electric System (Wuxi) Technology Co., Ltd, Wuxi 214000, China (e-mail: shaoshiyi@cssc-ses.com)

Youguang Guo is with the School of Electrical and Data Engineering, University of Technology Sydney, NSW 2007, Australia (e-mail: youguang.guo-1@uts.edu.au).

NOMENCLATURE

p_p, p_c	Pole pair numbers of power winding (PW) and control winding (CW).
ω_p, ω_c	Actual angular frequencies of PW and CW.
$\Delta\hat{\omega}_p$, $\hat{\omega}_p$, ω_p^*	Frequency error, estimation frequency and reference frequency of the PW fundamental voltage vector.
$\hat{\theta}_p$, θ_c^*	Estimation angle of the PW fundamental voltage vector and reference angle of the CW current vector.
$\boldsymbol{U}, \boldsymbol{I}, \boldsymbol{\psi}$	Voltage, current and flux vectors.
u, i, ψ	Voltage and current and flux scalars.
T_e	Total torque.
$s, \int$	Differential and integral operators.
R, L	Resistance and inductance.
Im	Imaginary part.
sup	The supremum of a function.
Inf	The infimum of a function.
n, v	Natural numbers from 1.
N	Iterations.
plus	The objective function value calculated by adding a small perturbation.
minus	The objective function value calculated by reducing a small disturbance.
λ_1, λ_2	Lagrange multiplier.
Superscript:	
~	Conjugate operator.
*	Reference value.
Subscript:	
p, c, r	PW, CW and rotor winding variables.
a, b, c	a-, b- and c-phase variables.
$d, q, 0$	d-, q-, and 0-axis components.
α, β	α- and β-axis components.
+, -	positive- and negative-sequence components.

I. INTRODUCTION

THE dc microgrid has been extensively researched over the last decade for its prominent advantages such as higher efficiency, no reactive power flow and natural interface with energy sources compared to the ac microgrid [1], [2], [3]. Among numerous dc power generation topologies, the brushless doubly-fed induction generator-dc (BDFIG-DC) system with the single converter-based topology shown in Fig. 1 has attracted attention from some scholars for its low cost and simple control [4], [5]. As illustrated in Fig. 1, the power winding (PW) and control winding (CW) of the BDFIG are connected to the three-phase diode rectifier (TDR) and the machine side convertor (MSC), respectively. The power can be transmitted to the grid or load from the dc bus, which means that the BDFIG-DC system can operate in grid-connected or standalone modes.

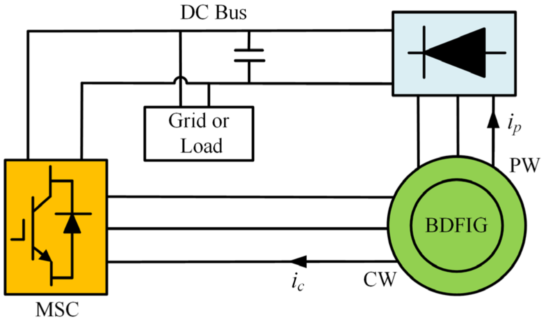

Fig. 1. Basic structure of the BDFIG-DC power generation system.

With the increase of operation time, the probability of dc microgrid failure also tends to rise, especially in harsh environments such as deserts, island and offshore [6], [7], [8]. Among all types of faults, the open-phase fault of the generator stator windings is one of the most common faults and usually caused by the bonding wires lifting in semiconductors, connector loosening, and overcurrent fusing [9], [10], [11]. In particular, for the BDFIG with dual electrical ports [12], the open-phase fault should be paid more attention. The open-phase fault can lead to significant three-phase unbalance in the stator winding and generate severe torque ripple, which causes high vibration and noise, deteriorating the operation stability of the BDFIG-DC system. In some special applications, it is necessary for the generator in fault to continue operating for a period. Usually, the open-phase fault does not trigger drastic fluctuations in output dc voltage because of the large capacitors installed on the dc bus in the dc microgrid, thereby ensuring a certain level of power output capability during the fault operation. Hence, minimizing torque ripple has become the primary task of the BDFIG-DC system for the fault-tolerant operation under the open-phase fault.

Some scholars have conducted research on suppressing torque ripple in the BDFIG-DC system. In [13] and [14], the torque ripple suppression method based on harmonic current injection is proposed. In [15], the torque ripple suppression method considering winding harmonic loss is presented. However, these methods developed in [13]-[15] are all for eliminating the torque ripple caused by TDR during the normal operation.

Unfortunately, few researches on the torque ripple suppression of the open-phase fault in the BDFIG-DC system are investigated currently. Therefore, it is necessary to draw upon fault-tolerant strategies and control methods from other dc power generation systems under the open-phase fault. The present works can be divided into two categories. The first category is to improve the system topology or machine structure. In [16], [17], [18] and [19], the topologies of power electronic converters are improved to suppress the torque ripple. The converter structures presented in [16] and [17] are equipped with redundant bridge arms, which ensures that the system’s topology and control strategy remain essentially unchanged before and after the fault occurs, thus preserving the original electrical performance to the greatest extent possible. The converter topologies proposed in [18] and [19] need to be constructed by the neutral point of the capacitor, which results that the control strategy needs to be adjusted before and after the fault occurs. In [20], a dc power generation system based on a five-phase dual-stator induction generator is proposed, which performs a reduced order transformation to obtain the *d*- and *q*-axis voltage and current correction values when a stator winding open-phase fault is detected. Although the methods in [16]-[20] can enhance the fault-tolerance ability of the dc power generation system, they all need to add external devices, which increases the system’s cost. The second category of torque ripple suppression strategies is to improve the control algorithm. In [21], [22], [23] and [24], the fault-tolerant method based on voltage space vector control for inverters is proposed, which compensates for the faulty space voltage vectors by modifying the modulation strategy of the original three-phase six-switch rectifier topology, enabling fault-tolerant operation of the inverter under single-switch open-circuit faults. However, the control methods proposed in [21]-[24] rely on the freewheeling effect of the parallel diode of the faulty switching device and are not advisable in the BDFIG-DC system under the PW open-phase fault.

Although these research works in [16]-[24] can cope with the torque ripple under the open-phase fault, they are difficult to be applied for the BDFIG-DC system due to some issues mentioned above. Therefore, it is necessary to develop a minimum torque ripple control strategy for the BDFIG-DC system under the open-phase fault. In this article, only the PW open-phase fault is discussed and the torque ripple minimization control strategy without external devices is proposed.

The rest of this article is organized as follows. In Section II, the torque harmonic components for the normal operation and PW open-phase fault are analyzed. The principle of minimizing the torque ripple under the PW open-phase fault is proposed in Section III. The design process of the control system is described in Section IV, while the comprehensive experimental results are illustrated in Section V. Finally, Section VI concludes this article.

II. Analysis of Torque Harmonic Components for Normal Operation and PW Open-phase Fault

A. Analysis of Torque Harmonic Components for Normal Operation

The harmonic dynamic mathematical models of BDFIG in the *dq* frame can be expressed as [14]

$$\boldsymbol{U}_{ph}^{h} = R_p \boldsymbol{I}_{ph}^{h} + s\boldsymbol{\psi}_{ph}^{h} + jh\omega_p \boldsymbol{\psi}_{ph}^{h} \tag{1}$$

$$\boldsymbol{\psi}_{ph}^{h} = L_p \boldsymbol{I}_{ph}^{h} + L_{pr} \boldsymbol{I}_{rh}^{h} \tag{2}$$

$$\boldsymbol{U}_{ch}^{h} = R_c \boldsymbol{I}_{ch}^{h} + s\boldsymbol{\psi}_{ch}^{h} + j(h\omega_p - (p_p + p_c)\omega_r)\boldsymbol{\psi}_{ch}^{h} \tag{3}$$

$$\boldsymbol{\psi}_{ch}^{h} = L_c \boldsymbol{I}_{ch}^{h} + L_{cr} \boldsymbol{I}_{rh}^{h} \tag{4}$$

$$0 = R_r \boldsymbol{I}_{rh}^{h} + s\boldsymbol{\psi}_{rh}^{h} + j(h\omega_p - p_p\omega_r)\boldsymbol{\psi}_{rh}^{h} \tag{5}$$

$$\boldsymbol{\psi}_{rh}^{h} = L_r \boldsymbol{I}_{rh}^{h} + L_{cr} \boldsymbol{I}_{ch}^{h} + L_{pr} \boldsymbol{I}_{ph}^{h} \tag{6}$$

where the superscript h represents the frequency order of the dq frame, and the subscript h represents the frequency order of the physical quantity. When the physical quantity is a negative-sequence component, h is a negative number.

The asynchronous torque generated by the rotor resistance is usually ignored [13], and the torque expression can be simplified to

$$T_e = 1.5(p_p + p_c)\mathrm{Im}(\tilde{\boldsymbol{\psi}}_p \boldsymbol{I}_p)\,. \tag{7}$$

When the system operates under the normal condition, considering the -5th and 7th harmonic components caused by the TDR, the torque expression can be expanded as

$$\begin{aligned} T_e = {} & 1.5\left(p_p + p_c\right) \\ & \mathrm{Im}\left[\left(\tilde{\boldsymbol{\psi}}_{p1}^{1} + \tilde{\boldsymbol{\psi}}_{p-5}^{-5} e^{j6\omega_p t} + \tilde{\boldsymbol{\psi}}_{p7}^{7} e^{-j6\omega_p t}\right)\right. \\ & \left.\left(\boldsymbol{I}_{p1}^{1} + \boldsymbol{I}_{p-5}^{-5} e^{-j6\omega_p t} + \boldsymbol{I}_{p7}^{7} e^{j6\omega_p t}\right)\right]. \end{aligned} \tag{8}$$

It is seen that Eq. (8) can be further written as

$$T_e = T_{e0} + T_{e6} + T_{e12} \tag{9}$$

where T_{e0}, T_{e6} and T_{e12} can be described by

$$\begin{cases} T_{e0} = 1.5\left(p_p + p_c\right)\mathrm{Im}\left(\tilde{\boldsymbol{\psi}}_{p1}^{1}\boldsymbol{I}_{p1}^{1} + \tilde{\boldsymbol{\psi}}_{p-5}^{-5}\boldsymbol{I}_{p-5}^{-5} + \tilde{\boldsymbol{\psi}}_{p7}^{7}\boldsymbol{I}_{p7}^{7}\right) \\ T_{e6} = 1.5\left(p_p + p_c\right)\mathrm{Im}\left(\tilde{\boldsymbol{\psi}}_{p1}^{1}\boldsymbol{I}_{p-5}^{-5} e^{-j6\omega_p t} + \tilde{\boldsymbol{\psi}}_{p7}^{7}\boldsymbol{I}_{p1}^{1} e^{-j6\omega_p t}\right. \\ \qquad \left. + \tilde{\boldsymbol{\psi}}_{p1}^{1}\boldsymbol{I}_{p7}^{7} e^{j6\omega_p t} + \tilde{\boldsymbol{\psi}}_{p-5}^{-5}\boldsymbol{I}_{p1}^{1} e^{j6\omega_p t}\right) \\ T_{e12} = 1.5(p_p + p_c)\,\mathrm{Im}\left(\tilde{\boldsymbol{\psi}}_{p-5}^{-5}\boldsymbol{I}_{p7}^{7} e^{j12\omega_p t} + \tilde{\boldsymbol{\psi}}_{p7}^{7}\boldsymbol{I}_{p-5}^{-5} e^{-j12\omega_p t}\right) \end{cases} .(10)$$

According to (9) and (10), the torque harmonic components during the normal operation are primarily the 6th and 12th harmonic torques, and the 12th torque harmonic component is often be neglected for its smaller proportion [14].

B. *Analysis of Torque Harmonic Components for PW Open-Phase Fault*

The BDFIG-DC system with the PW open-phase fault is illustrated in Fig. 2. The two normal phases of PW, along with the TDR, can form a single-phase uncontrolled rectifier circuit.

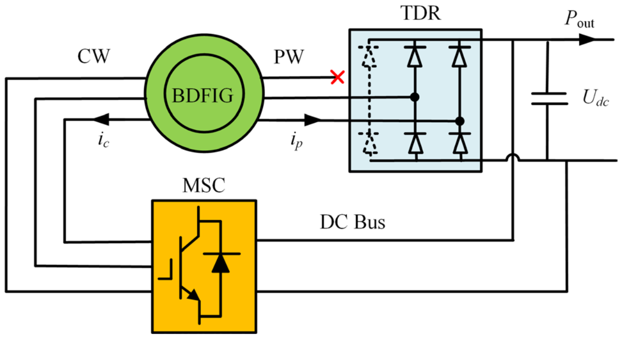

Fig. 2. System structure under the PW open-phase fault.

In this faulty system, the harmonic components on the ac side conform to the following patterns [26]:

1) The harmonic orders are odd.

2) As the harmonic order increases, the amplitude of the harmonic component decreases.

Fig. 3 illustrates the main harmonic analyses of the PW flux, PW voltage and PW current in the normal operation and PW open-phase fault with the rated load, which matches the above patterns of harmonic components presented in [26]. Besides, compared to the normal operation, there are significant increases in the 3rd harmonic components of the PW flux, PW voltage and PW current under the PW open-phase fault.

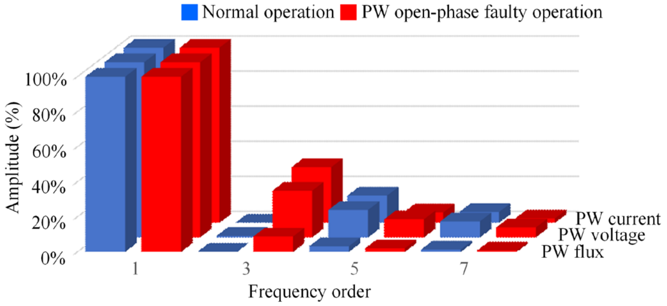

Fig. 3. Main harmonic analyses of PW flux, PW voltage and PW current in the normal operation and PW open-phase fault with the rated load.

During the PW open-phase fault, the two normal phases of PW form the current loop that results in a pulsating magnetic field, leading to a pulsating magnetic potential. According to the theory of double-revolving magnetic fields, the pulsating magnetic potential can be decomposed into two components: the forward magnetic potential and the reverse magnetic potential with the same magnitude, opposite direction and identical rotational speed. The presence of the forward and the reverse magnetic potential results in the occurrence of both positive and negative sequence harmonic components in PW. Therefore, the PW flux and current under the open-phase fault in the dq frame can be expressed as

$$\boldsymbol{\psi}_p = \sum_{v=1}^{n}\left(\boldsymbol{\psi}_{p(2v-1)}^{(2v-1)} e^{j(2v-2)\omega_p t} + \boldsymbol{\psi}_{p-(2v-1)}^{-(2v-1)} e^{-j2v\omega_p t}\right) \tag{11}$$

$$\boldsymbol{I}_p = \sum_{v=1}^{n}\left(\boldsymbol{I}_{p(2v-1)}^{(2v-1)} e^{j(2v-2)\omega_p t} + \boldsymbol{I}_{p-(2v-1)}^{-(2v-1)} e^{-j2v\omega_p t}\right) \tag{12}$$

where the superscript 2v-1 represents the frequency order of the synchronous rotating frame, and the subscript 2v-1 represents the frequency order of the physical quantity.

Substituting (11) and (12) into (7), the torque expression under the PW open-phase fault can be expanded to

$$\begin{aligned} T_e = {} & 1.5\left(p_p + p_c\right) \\ & \mathrm{Im}\left[\left(\sum_{v=1}^{n}(\tilde{\boldsymbol{\psi}}_{p(2v-1)}^{(2v-1)} e^{-j(2v-2)\omega_p t} + \tilde{\boldsymbol{\psi}}_{p-(2v-1)}^{-(2v-1)} e^{j2v\omega_p t})\right)\right. \\ & \left.\left(\sum_{v=1}^{n}(\boldsymbol{I}_{p(2v-1)}^{(2v-1)} e^{j(2v-2)\omega_p t} + \boldsymbol{I}_{p-(2v-1)}^{-(2v-1)} e^{-j2v\omega_p t})\right)\right]. \end{aligned} \tag{13}$$

Based on the relationship between the PW flux and voltage depicted in (1), ignoring the PW resistance and the differential term, the PW flux can be expressed by the PW voltage as

$$\boldsymbol{\psi}_{ph}^{h}=\frac{\boldsymbol{U}_{ph}^{h}}{jh\omega_p}. \tag{14}$$

Substituting (14) into (13), the torque expression can be rewritten as

$$\begin{aligned}T_e&=1.5\left(p_p+p_c\right)\\&\mathrm{Im}\left[\left(\sum_{v=1}^{n}\left(\frac{\boldsymbol{j}\tilde{\boldsymbol{U}}_{p(2v-1)}^{(2v-1)}}{(2v-1)\omega_p}e^{-j(2v-2)\omega_p t}-\frac{\boldsymbol{j}\tilde{\boldsymbol{U}}_{p-(2v-1)}^{-(2v-1)}}{(2v-1)\omega_p}e^{j2v\omega_p t}\right)\right)\right.\\&\left.\left(\sum_{v=1}^{n}\left(\boldsymbol{I}_{p(2v-1)}^{(2v-1)}e^{j(2v-2)\omega_p t}+\boldsymbol{I}_{p-(2v-1)}^{-(2v-1)}e^{-j2v\omega_p t}\right)\right)\right]\end{aligned} \tag{15}$$

where the PW voltage and current vectors can be expressed by their *d*- and *q*-axis components as

$$\begin{cases}\boldsymbol{U}_{p(2v-1)}^{(2v-1)}=u_{pd(2v-1)}^{(2v-1)}+ju_{pq(2v-1)}^{(2v-1)}\\\boldsymbol{U}_{p-(2v-1)}^{-(2v-1)}=u_{pd-(2v-1)}^{-(2v-1)}+ju_{pq-(2v-1)}^{-(2v-1)}\\\boldsymbol{I}_{p(2v-1)}^{(2v-1)}=i_{pd(2v-1)}^{(2v-1)}+ji_{pq(2v-1)}^{(2v-1)}\\\boldsymbol{I}_{p-(2v-1)}^{-(2v-1)}=i_{pd-(2v-1)}^{-(2v-1)}+ji_{pq-(2v-1)}^{-(2v-1)}\end{cases}. \tag{16}$$

In practical applications, it is difficult to directly calculate the torque of the faulty system from (15), because numerous harmonic components with different orders are involved in (15).

Fortunately, as depicted in Fig. 3, the proportion of the PW harmonic flux under the PW open-phase fault is relatively small. Therefore, to simplify the analysis, the harmonic components of the PW flux can be ignored when calculating the PW torque. Consequently, Eq. (15) can be simplified as

$$\begin{aligned}T_e&=1.5\left(p_p+p_c\right)\\&\mathrm{Im}\left[\left(\frac{\boldsymbol{j}\tilde{\boldsymbol{U}}_{p1}^{1}}{\omega_p}-\frac{\boldsymbol{j}\tilde{\boldsymbol{U}}_{p-1}^{-1}}{\omega_p}e^{j2\omega_p t}\right)\right.\\&\left.\left(\sum_{v=1}^{n}\left(\boldsymbol{I}_{p(2v-1)}^{(2v-1)}e^{j(2v-2)\omega_p t}+\boldsymbol{I}_{p-(2v-1)}^{-(2v-1)}e^{-j2v\omega_p t}\right)\right)\right].\end{aligned} \tag{17}$$

For further simplification of (17), the phase-locked loop (PLL) is applied to track the fundamental voltage vector of PW. The schematic diagram of the PLL is illustrated in Fig. 4.

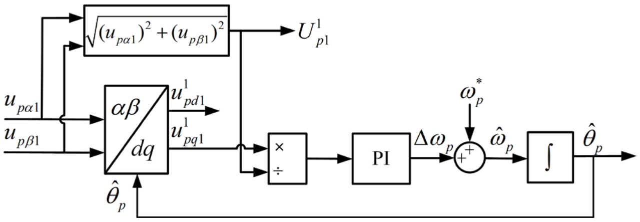

Fig. 4. Structure of PLL for tracking the PW fundamental voltage vector.

As a result, the *q*-axis component of the PW fundamental voltage vector converges to zero in steady state, resulting in the absolute value of the *d*-axis component being equal to the amplitude of the voltage vector, which means

$$\begin{cases}u_{pd1}^{1}=U_{p1}^{1}\\u_{pq1}^{1}=0\end{cases} \tag{18}$$

where U_{p1}^{1} represents the amplitude of the PW fundamental voltage vector.

Moreover, assuming that phase-*a* of PW is the faulty phase, the PW three-phase currents can be expressed as

$$\begin{cases}i_{pa}=0\\i_{pb}=-i_{pc}\end{cases}. \tag{19}$$

The unbalanced PW three-phase currents shown in (19) can be decomposed into positive- and negative-sequence components as follows

$$\begin{bmatrix}i_{pa+}\\i_{pb+}\\i_{pc+}\end{bmatrix}=\frac{1}{3}\begin{bmatrix}1&e^{j2\pi/3}&e^{j4\pi/3}\\e^{j4\pi/3}&1&e^{j2\pi/3}\\e^{j2\pi/3}&e^{j4\pi/3}&1\end{bmatrix}\begin{bmatrix}i_{pa}\\i_{pb}\\i_{pc}\end{bmatrix} \tag{20}$$

$$\begin{bmatrix}i_{pa-}\\i_{pb-}\\i_{pc-}\end{bmatrix}=\frac{1}{3}\begin{bmatrix}1&e^{j4\pi/3}&e^{j2\pi/3}\\e^{j2\pi/3}&1&e^{j4\pi/3}\\e^{j4\pi/3}&e^{j2\pi/3}&1\end{bmatrix}\begin{bmatrix}i_{pa}\\i_{pb}\\i_{pc}\end{bmatrix} \tag{21}$$

where the subscripts "+" and "-" represent the positive- and negative-sequence components, respectively.

Substituting (19) to (20) and (21), the relationship of positive- and negative-sequence components of PW three-phase currents can be expressed as

$$i_{pa+}=-i_{pa-},\ i_{pb+}=-i_{pc-},\ i_{pc+}=-i_{pb-}. \tag{22}$$

Since only the fundamental and odd harmonic components are involved in the PW currents under the PW open-phase fault, the positive- and negative-sequence components of the PW three-phase currents can be further expanded as

$$\begin{cases}i_{pa+}=\sum_{v=1}^{n}i_{pa(2v-1)},\ i_{pa-}=\sum_{v=1}^{n}i_{pa-(2v-1)}\\i_{pb+}=\sum_{v=1}^{n}i_{pb(2v-1)},\ i_{pb-}=\sum_{v=1}^{n}i_{pb-(2v-1)}\\i_{pb+}=\sum_{v=1}^{n}i_{pb(2v-1)},\ i_{pb-}=\sum_{v=1}^{n}i_{pb-(2v-1)}\end{cases}. \tag{23}$$

It can be seen that according to (22), the fundamental and odd harmonic components in (23) should satisfy the relationship as follows:

$$i_{pa(2v-1)}=-i_{pa-(2v-1)},\ i_{pb(2v-1)}=-i_{pc-(2v-1)},\ i_{pc(2v-1)}=-i_{pb-(2v-1)}. \tag{24}$$

Transforming the fundamental and these odd harmonics in (23) from the *abc* frame into *dq* frame of the corresponding order, Eq. (24) can be further rewritten as

$$\begin{cases}i_{pd(2v-1)}^{(2v-1)}=-i_{pd-(2v-1)}^{-(2v-1)}\\i_{pq(2v-1)}^{(2v-1)}=i_{pq-(2v-1)}^{-(2v-1)}\end{cases} \tag{25}$$

where the detailed transformation matrixes can be found in (A1) and (A2) of the Appendix.

Substituting (16), (18) and (25) to (17), Eq. (17) can be expressed as

$$T_{e\_ud}=1.5\frac{p_p+p_c}{\omega_p}\left(\begin{array}{c}\left(u_{pd1}^{1}+u_{pd-1}^{-1}\right)i_{pd1}^{1}-u_{pq-1}^{-1}i_{pq1}^{1}\\ +\sum_{v=1}^{n}\begin{pmatrix}\left(i_{pd(2v+1)}^{(2v+1)}-i_{pd(2v-1)}^{(2v-1)}\right)\\ \left(u_{pd1}^{1}+u_{pd-1}^{-1}\right)\end{pmatrix}\cos(2v\omega_p t)\\ -\sum_{v=1}^{n}\begin{pmatrix}\left(i_{pq(2v+1)}^{(2v+1)}-i_{pq(2v-1)}^{(2v-1)}\right)\\ u_{pq-1}^{-1}\end{pmatrix}\cos(2v\omega_p t)\\ +\sum_{v=1}^{n}\begin{pmatrix}\left(i_{pq(2v-1)}^{(2v-1)}-i_{pq(2v+1)}^{(2v+1)}\right)\\ \left(u_{pd1}^{1}+u_{pd-1}^{-1}\right)\end{pmatrix}\sin(2v\omega_p t)\\ -\sum_{v=1}^{n}\begin{pmatrix}\left(i_{pd(2v-1)}^{(2v-1)}-i_{pd(2v+1)}^{(2v+1)}\right)\\ u_{pq-1}^{-1}\end{pmatrix}\sin(2v\omega_p t)\end{array}\right).\quad(26)$$

It is seen that Eq. (26) can be further divided into

$$T_e=T_{e\_ud}+T_{e\_uq}\quad(27)$$

where the expressions of T_{e_ud} and T_{e_uq} can be described by

$$T_{e\_ud}=1.5\frac{p_p+p_c}{\omega_p}(u_{pd1}^{1}+u_{pd-1}^{-1})\left(\begin{array}{l}i_{pd1}^{1}+\sum_{v=1}^{n}(i_{pd(2v+1)}^{(2v+1)}-i_{pd(2v-1)}^{(2v-1)})\cos(2v\omega_p t)\\ +\sum_{v=1}^{n}(i_{pq(2v-1)}^{(2v-1)}-i_{pq(2v+1)}^{(2v+1)})\sin(2v\omega_p t)\end{array}\right)\quad(28)$$

$$T_{e\_uq}=-1.5\frac{p_p+p_c}{\omega_p}u_{pq-1}^{-1}\left(\begin{array}{l}i_{pq1}^{1}+\sum_{v=1}^{n}(i_{pq(2v+1)}^{(2v+1)}-i_{pq(2v-1)}^{(2v-1)})\cos(2v\omega_p t)\\ +\sum_{v=1}^{n}(i_{pd(2v-1)}^{(2v-1)}-i_{pd(2v+1)}^{(2v+1)})\sin(2v\omega_p t)\end{array}\right).\quad(29)$$

Fig. 5 displays the torque waveforms obtained during the normal operation and the PW open-phase fault, respectively, utilizing (28), (29) and the torque expression provided in [27]. It can be observed that T_{e_ud} represents the main proportion of the torque expression in (27) and well matches the widely used BDFIG torque formula presented in [27]. Therefore, the analysis of the torque should be focused on T_{e_ud}.

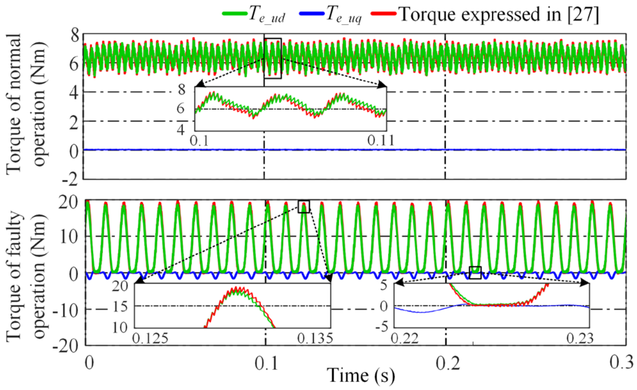

Fig. 5. Torque waveforms obtained from T_{e_ud}, T_{e_uq} and the torque expression presented in [27] during the normal operation and PW open-phase fault.

In addition, the amplitudes of harmonics decrease along with the increase of harmonic order, so that the high-order harmonic currents in PW are close to zero. As a result, it can be derived that

$$\begin{cases}\sum_{v=1}^{n}(i_{pd(2v+1)}^{(2v+1)}-i_{pd(2v-1)}^{(2v-1)})\approx -i_{pd1}^{1}\\ \sum_{v=1}^{n}(i_{pq(2v-1)}^{(2v-1)}-i_{pq(2v+1)}^{(2v+1)})\approx i_{pq1}^{1}\end{cases}.\quad(30)$$

From (28), (30) and Fig. 5, it is noted that there are some moments when the T_{e_ud} reaches zero during the PW open-phase fault, which can be expressed as

$$T_{e\_ud}\approx 0\ \text{ when } t=\frac{k\pi}{2\omega_p},\ k=0,1,2\ldots.\quad(31)$$

Since T_{e_ud} accounts for the major part of the torque, the total torque under the PW open-phase fault has the similar feature as T_{e_ud} presented in (31).

III. PRINCIPLE OF MINIMIZING TORQUE RIPPLE UNDER PW OPEN-PHASE FAULT

From (28), the harmonic torque can be expressed as

$$T_{e\_h}=1.5\frac{p_p+p_c}{\omega_p}(u_{pd1}^{1}+u_{pd-1}^{-1})\left(\begin{array}{l}\sum_{v=1}^{n}(i_{pd(2v+1)}^{(2v+1)}-i_{pd(2v-1)}^{(2v-1)})\cos(2v\omega_p t)\\ +\sum_{v=1}^{n}(i_{pq(2v-1)}^{(2v-1)}-i_{pq(2v+1)}^{(2v+1)})\sin(2v\omega_p t)\end{array}\right).\quad(32)$$

In order to minimize the torque ripple generated by the open-phase fault in PW, Eq. (32) needs to approach zero, which means

$$\begin{cases}\sum_{v=1}^{n}(i_{pd(2v+1)}^{(2v+1)}-i_{pd(2v-1)}^{(2v-1)})\cos(2v\omega_p t)=0\\ \sum_{v=1}^{n}(i_{pq(2v-1)}^{(2v-1)}-i_{pq(2v+1)}^{(2v+1)})\sin(2v\omega_p t)=0\end{cases}.\quad(33)$$

Then, Eq. (33) can be further derived as

$$\begin{cases}i_{pd1}^{1}=i_{pd3}^{3}=i_{pd5}^{5}=i_{pd7}^{7}=\ldots=i_{pd(2v-1)}^{(2v-1)}\\ i_{pq1}^{1}=i_{pq3}^{3}=i_{pq5}^{5}=i_{pq7}^{7}=\ldots=i_{pq(2v-1)}^{(2v-1)}\end{cases}.\quad(34)$$

However, Eq. (34) is impossible to be satisfied, because the *d*- and *q*-axis components of all the PW harmonic currents are required to be equal to those of the PW fundamental current.

Although it is not possible to completely eliminate the torque ripple under the PW open-phase fault, it is feasible to minimize the torque ripple by regulating the PW harmonic currents. For obtaining the optimal PW harmonic current references to minimize the torque ripple, it is necessary to construct the objective function F_{phc} as follows:

$$F_{phc}=\left(\begin{array}{l}\sum_{v=1}^{n}(i_{pd(2v+1)}^{(2v+1)}-i_{pd(2v-1)}^{(2v-1)})\cos(2v\omega_p t)\\ +\sum_{v=1}^{n}(i_{pq(2v-1)}^{(2v-1)}-i_{pq(2v+1)}^{(2v+1)})\sin(2v\omega_p t)\end{array}\right).\quad(35)$$

The function F_{phc} represents the PW harmonic currents associated with the torque ripple in (32). To minimize the torque ripple under the PW open-phase fault, the fluctuation of the function F_{phc} should be minimized, i.e.,

$$\text{minimize}\left\{\sup(F_{phc})-\inf(F_{phc})\right\}. \tag{36}$$

To achieve (36), the PW harmonic currents Lagrange function L_{phc} has to be constructed as

$$\begin{aligned} L_{phc} &= \sup(F_{phc})-\inf(F_{phc})+\lambda_1\Big(\sum_{v=1}^{n}(i_{pd(2v+1)}^{(2v+1)}-i_{pd(2v-1)}^{(2v-1)})+i_{pd1}^{1}\Big) \\ &\quad +\lambda_2\Big(\sum_{v=1}^{n}(i_{pq(2v-1)}^{(2v-1)}-i_{pq(2v+1)}^{(2v+1)})-i_{pq1}^{1}\Big). \end{aligned} \tag{37}$$

By differentiating the variables contained in (37) and setting the derivative to zero, the result can be expressed as

$$\begin{cases} \dfrac{dL_{phc}}{d\lambda_1}=0,\ \dfrac{dL_{phc}}{d\lambda_2}=0 \\ \dfrac{dL_{phc}}{di_{pd(2v+1)}^{(2v+1)}}=0,\ v=1,2,3\cdots n \\ \dfrac{dL_{phc}}{di_{pq(2v+1)}^{(2v+1)}}=0,\ v=1,2,3\cdots n \end{cases}. \tag{38}$$

However, due to the absence of the analytical expression for sup(F_{phc})-inf(F_{phc}) in L_{phc} and (38) consisting of $2n$+2 nonlinear equations, it is difficult to find an analytical solution for (38). Consequently, a numerical solution should be considered. To simplify the computation, the PW harmonic currents with the order exceeding five are neglected, so that (35) can be rewritten as

$$\begin{aligned} F_{phc} &= k_1\cos(2\omega_p t)+k_2\cos(4\omega_p t)+k_3\cos(6\omega_p t) \\ &\quad +g_1\sin(2\omega_p t)+g_2\sin(4\omega_p t)+g_3\sin(6\omega_p t) \end{aligned} \tag{39}$$

where k_1, k_2, k_3 and g_1, g_2, g_3 are defined as

$$\begin{cases} k_1=i_{pd3}^{3}-i_{pd1}^{1},\ k_2=i_{pd5}^{5}-i_{pd3}^{3},\ k_3=-i_{pd5}^{5} \\ g_1=i_{pq1}^{1}-i_{pq3}^{3},\ g_2=i_{pq3}^{3}-i_{pq5}^{5},\ g_3=i_{pq5}^{5} \end{cases}. \tag{40}$$

From (30), these coefficients in (39) also satisfy

$$\begin{cases} k_1+k_2+k_3=-i_{pd1}^{1} \\ g_1+g_2+g_3=i_{pq1}^{1} \end{cases}. \tag{41}$$

From (40), the reference values of the PW harmonic currents can be calculated by k_1, k_2, k_3 and g_1, g_2, g_3. Hence, once the values of the coefficients k_1, k_2, k_3 and g_1, g_2, g_3 satisfy (36), the corresponding reference values of the PW harmonic currents can minimize the torque ripple.

To find the coefficients k_1, k_2, k_3 and g_1, g_2, g_3 satisfying (36), the Newton's gradient descent method is utilized for the numerical iterative solution. The specific iterative procedure for k_1 can be illustrated in Fig. 6. The perturbation represents a small change in k_1. In addition, for calculating the gradient for k_1, two perturbations (the incremental perturbation and the decremental perturbation) are applied to k_1, and then the central difference method is employed to estimate the gradient. In each iteration, k_1 is updated by multiplying the current gradient by the learning rate. In order to prevent the algorithm from diverging, the maximum value of k_1 should be set. Usually, the content of harmonic current should be less than that of the fundamental current, so that the maximum value of k_1 can be set as zero according to (40). The iterative procedures for k_2, g_1 and g_2 are similar to that presented in Fig. 6. Besides, k_3 and g_3 can be derived from (41) with the obtained values of k_1, k_2 and g_1, g_2.

In order to accelerate the convergence speed of iterations, the initial values of k_1, k_2, k_3 and g_1, g_2, g_3 are determined offline using the function *fmincon* in MATLAB, which approximately satisfy

$$\begin{cases} k_1=-\dfrac{1}{2}i_{pd1}^{1},\ k_2=-\dfrac{1}{3}i_{pd1}^{1},\ k_3=-\dfrac{1}{6}i_{pd1}^{1} \\ g_1=0.3i_{pq1}^{1},\ g_2=0.4i_{pq1}^{1},\ g_3=0.3i_{pq1}^{1} \end{cases}. \tag{42}$$

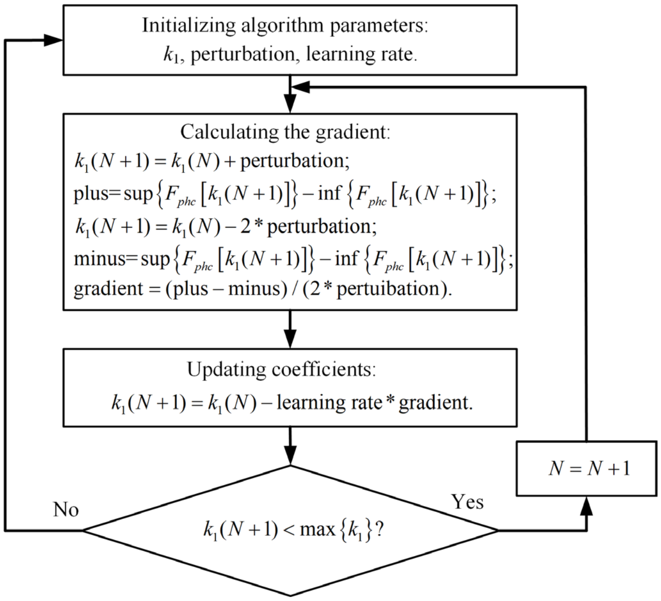

Fig. 6. Iterative procedure of the coefficient k_1 based on the Newton's gradient descent method.

These coefficients obtained by the numerical iterative solution can be used to calculate the real-time reference values of PW harmonic currents according to (40), i.e.,

$$\begin{cases} i_{pd3}^{3*}=-k_2-k_3,\ i_{pq3}^{3*}=g_2+g_3 \\ i_{pd5}^{5*}=-k_3,\ i_{pq5}^{5*}=g_3 \end{cases}. \tag{43}$$

IV. CONTROL STRATEGY DESIGN

A. Basic Control Strategy

The BDFIG-DC system can operate at grid-connected and standalone modes, for which the control objectives are the output power and dc bus voltage, respectively. The relationship between the two control objectives and the CW fundamental current can be expressed as [15]

$$P_{\text{out}}=\frac{3L_{pr}L_{cr}}{\pi(L_pL_r-(L_{pr})^2)}\frac{\omega_p+\omega_c}{\omega_p}U_{dc}i_{cd1}^{1} \tag{44}$$

$$U_{\mathrm{dc}}=\frac{\pi}{2}\left|\frac{\left(j\omega_p L_{pr}L_{cr}/L_r\right)Z_{\mathrm{load}}}{\left(R_p+j\omega_p\left(L_p-L_{pr}^2/L_r\right)\right)-Z_{\mathrm{load}}}\right|I_{cd1}^1 . \tag{45}$$

From (44) and (45), the *d*-axis component of the CW fundamental current can be obtained through the proportional-integral (PI) controller for the output power or dc bus voltage. Usually, the reference value for the *q*-axis component of the CW fundamental current is set to zero, resulting in the *d*-axis component of the CW fundamental current being equal to the amplitude of the CW fundamental current.

B. *PW Harmonic Current Control Strategy*

According to (1), (2) and (6), the linear relationship between the PW and CW currents can be expressed as

$$\begin{cases} i_{pdh}^h=\dfrac{L_{pr}L_{cr}}{L_pL_r-L_{pr}^2}i_{cdh}^h+\dfrac{L_r}{h\omega_p\left(L_pL_r-L_{pr}^2\right)}u_{pqh}^h \\ i_{pqh}^h=\dfrac{L_{pr}L_{cr}}{L_pL_r-L_{pr}^2}i_{cqh}^h-\dfrac{L_r}{h\omega_p\left(L_pL_r-L_{pr}^2\right)}u_{pdh}^h \end{cases} . \tag{46}$$

From (46), the PW harmonic current can be controlled by the corresponding CW harmonic current through the PI controller. The structure of the PW harmonic current control module is illustrated in Fig. 7. The reference values of the PW harmonic currents are calculated by (43), and the corresponding feedback values can be acquired through the multiple second-order generalized integrators (MSOGI) [28].

Since the reference values of the CW harmonic currents obtained from the PW harmonic current control module have been transformed into the *dq* frame of the CW fundamental current, they are ac quantities. The reference value of the total CW current would consist of both dc and ac quantities. Consequently, the proportional-integral-resonant (PIR) controller should be utilized to regulate the total CW currents. The transfer function of the employed PIR controller can be expressed as

$$\begin{aligned} G_{\mathrm{PIR}}=K_p+\frac{K_i}{s}+\frac{2K_{r1}\omega_{cut}s}{s^2+2\omega_{cut}s+(2\omega_p)^2} \\ +\frac{2K_{r2}\omega_{cut}s}{s^2+2\omega_{cut}s+(4\omega_p)^2} \end{aligned} \tag{47}$$

where K_p and K_i are the gains of proportional and integral controllers; ω_{cut} is the cutoff frequency, which is usually in the range of 5 to 15 rad/s [29], and it is chosen to be 10 rad/s in this article; K_{r1} and K_{r2} are the gains of resonant controllers.

From Fig. 7, it can be observed that the control of PW harmonic current does not rely on any machine parameters, so that the robustness of the control system can be significantly enhanced.

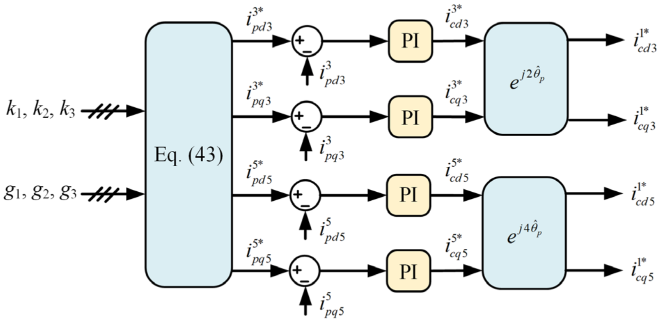

Fig. 7. Structure of the PW harmonic current control module.

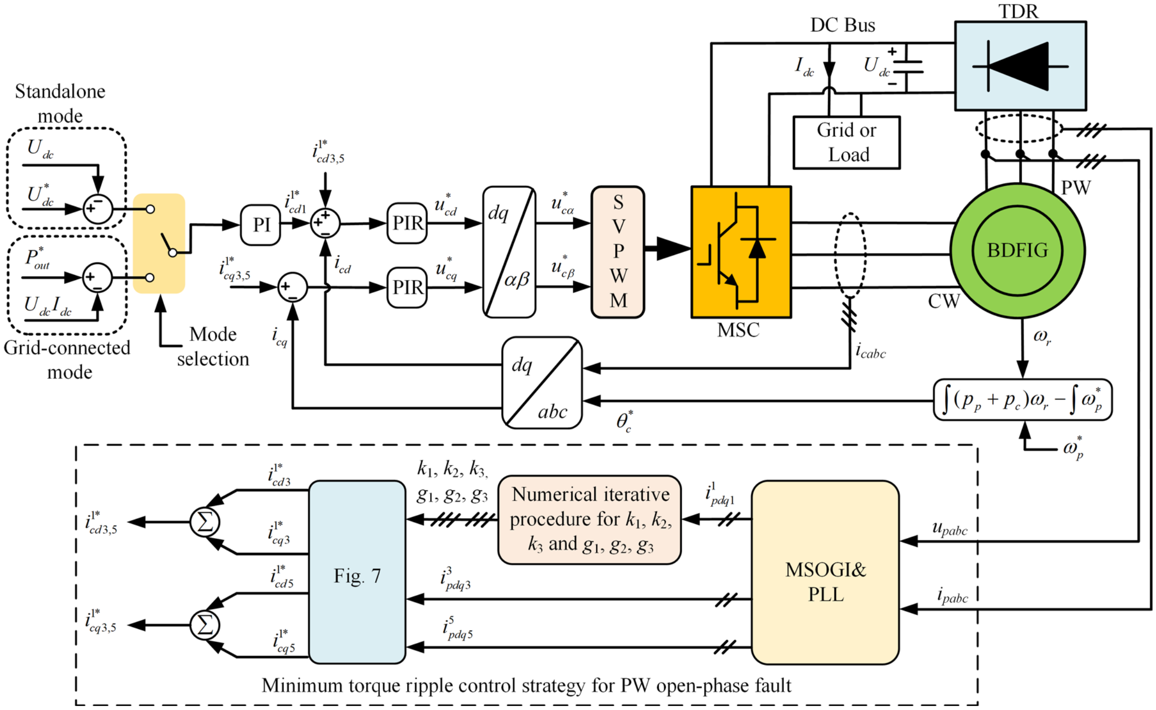

Fig. 8. Structure of the overall control strategy.

C. Overall Control Strategy

The overall control strategy is presented in Fig. 8. During the PW open-phase fault, the compensatory CW harmonic currents are generated by the proposed control strategy to minimize the torque ripple, so that the operation safety of the system can be enhanced. The CW fundamental current is utilized to regulate the system output power or the dc bus voltage. The numerical iterative procedure for k_1, k_2, k_3, and g_1, g_2, g_3 has been illustrated in Section III. And the PLL, PW harmonic current control module and MSOGI have also been presented in Sections II and IV-B.

V. EXPERIMENTAL AND SIMULATION RESULTS

A. Experimental Setup

To validate the effectiveness of the proposed control strategy, an experimental platform has been constructed as shown in Fig. 9. An 11-kW induction motor (IM) is utilized as the prime mover to drive the 5-kW BDFIG, and the main parameters of the BDFIG are listed in Table I. The contactor is connected to one phase of PW to switch between the normal operation and the open-phase fault. The MSC is under the control of the 32-bit floating-point DSP TMS320F28335. In the control program, the switching frequency is set to 5 kHz, and the control period is 0.2 ms. The 10000-μF dc bus capacitor is interposed between the MSC and the TDR. All the loads are linked to the dc bus. The current and voltage of the BDFIG can be sampled using the wave recorder MR6000 equipped with current and voltage probes.

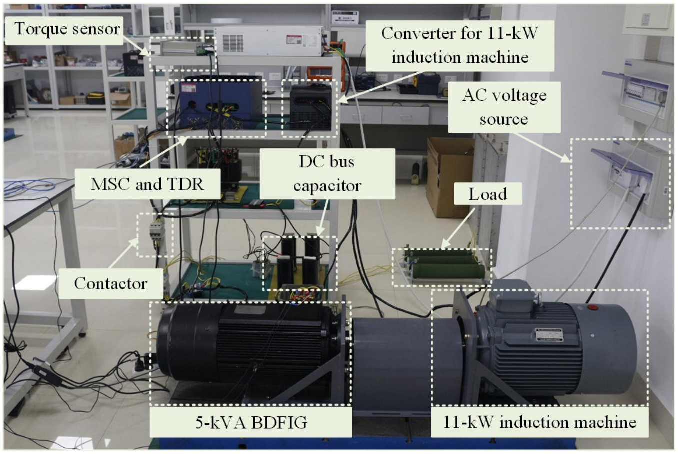

Fig. 9. Photograph of the experimental setup.

The selection of grid-connected and standalone modes only affects the reference value of the CW fundamental current, having no effect on that of the CW harmonic current. Therefore, only standalone mode is considered to validate the proposed strategy in this article. In all experiments, the dc bus voltage and PW frequency are set to 350 V and 50 Hz, respectively. The perturbation and learning rate for the Newton's gradient descent method is set to 0.0002 and 0.05, and the parameters K_p, K_i, K_{r1}, K_{r2} for the PIR controller are configured as 3, 8.5, 0.1, 0.1, respectively. The experiments are conducted in four typical operating scenarios, including sub-synchronous speed, super-synchronous speed, load change and speed change.

TABLE I
MAIN PARAMETERS OF THE 5-KVA BDFIG

Parameter	Value	Parameter	Value
PW pole pairs	1	R_p	2.43 Ω
CW pole pairs	3	R_c	1.78 Ω
PW rated power factor	0.8 (lag)	R_r	3.00 Ω
Natural synchronous speed	750 rpm	L_p	0.654 H
Speed range	600-1200 rpm	L_c	0.142 H
PW rated voltage	380 V	L_r	0.884 H
PW rated current	8 A	L_{pr}	0.635 H
CW rated voltage	0-180 V	L_{cr}	0.138 H
CW rated current	24 A	Rotor type	Wound rotor

B. Experimental Results at Sub-synchronous Speed

Fig. 10 illustrates the experimental results under the resistive load of 136 Ω and the sub-synchronous speed of 601 rpm. At the beginning, the system is in the normal operation condition. At 1.8 s, the phase-a of PW is disconnected, and the minimum torque ripple control strategy is activated at 3.2 s. The entire torque waveform and its detailed view are shown in Figs. 10(a)-(d). During the normal operation, the peak-to-peak value of the torque is 7.99 Nm. Due to the open-phase fault in PW, the peak-to-peak value of the torque rises to 44.33 Nm. After the proposed strategy is activated, the peak-to-peak value of the torque decreases to 23.29 Nm, reduced by 47.5% compared to that without strategy activation under the PW open-phase fault. Furthermore, from the detailed view of the torque in Figs. 10(c) and 10(d), it can be observed that the torque drops to zero every 10 ms, which is consistent with the results derived from (31). The harmonic analysis of the torque is displayed in Fig. 10(e). During the normal operation, the most significant harmonic component of the torque is the 6th harmonic, whose amplitude is 30.7% of the amplitude of the fundamental torque component. Under the PW open-phase fault without the minimum torque ripple control strategy, the contents of the torque 2nd and 4th harmonic components are significantly increased, reaching 122.0% and 12.6%, respectively. Meanwhile, the 6th harmonic component of the torque decreases to 7.6%. It should be noted that the 2nd harmonic component of the torque even surpasses the fundamental component, which is the main target of the torque ripple suppression. Upon activation of the proposed strategy, the 2nd harmonic component of the torque is reduced from 122.0% to 55.1%. However, the other even-order harmonic components of the torque are increased. It can also be observed from (32) that when the low-order even harmonics of the torque are reduced, it inevitably leads to an increase of the higher-order even harmonics. Fig. 10(f) illustrates the iterative procedure of the value of sup(F_{phc})-inf(F_{phc}) after the control strategy is activated. Once the initial values of the coefficients k_1, k_2, k_3 and g_1, g_2, g_3 are set according to (42), the value of sup(F_{phc})-inf(F_{phc}) can rapidly converge from 4.14 to 4.13. Due to the injection of the PW and CW harmonic currents, the amplitudes of the PW and CW currents, as shown in Figs. 10(g) and (i), are increased after the proposed control strategy is enabled. Figs. 10(h) and (j) illustrate the *d*- and *q*-axis components of the 3rd, -3rd, 5th and -5th PW harmonic currents, which matches the analysis in Sections II and III.

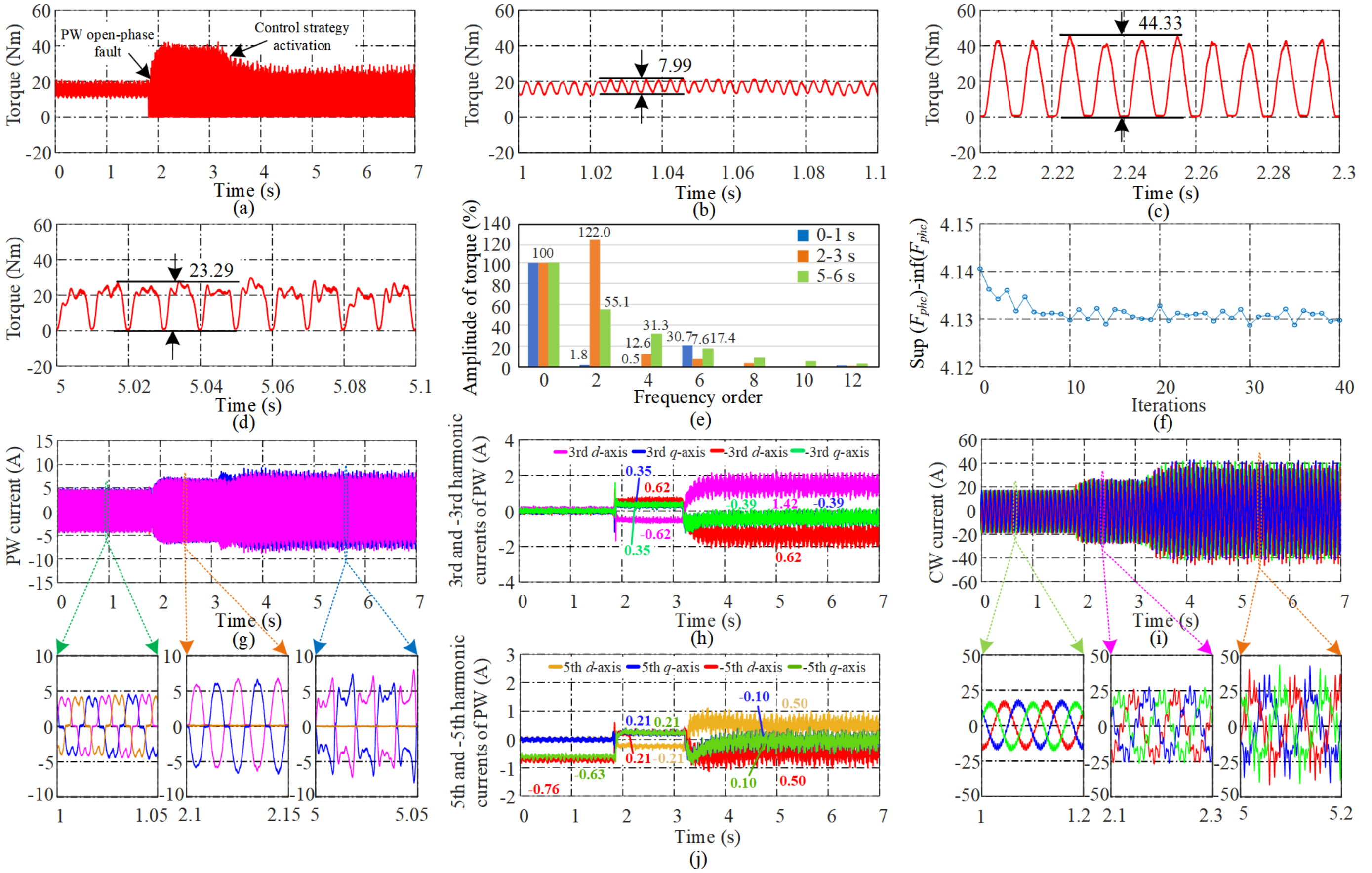

Fig. 10. Experimental results at sub-synchronous speed. (a) Torque. (b) Detailed view of the torque from 1 to1.1 s. (c) Detailed view of the torque from 2.2 to 2.3 s. (d) Detailed view of the torque from 5 to 5.1 s. (e) Harmonic analysis of the torque. (f) Value of sup(F_{phc})-inf(F_{phc}). (g) PW current. (h) *D*- and *q*-axis components of the PW 3rd and -3rd harmonic currents. (i) CW current. (j) *D*- and *q*-axis components of the PW 5th and -5th harmonic currents.

C. Experimental Results at Super-synchronous Speed

Fig. 11 presents the experimental results at the super-synchronous of 906 rpm with the resistive load of 74 Ω. The PW open-phase fault occurs at 2.2 s, and the minimum torque ripple control strategy is activated at 4.2 s. From Fig. 11(a)-(e), after the proposed control strategy is enabled, the torque peak-to-peak value is reduced by 46.6%. Meanwhile, the content of the torque 2nd harmonic decreases from 122.2% to 52.7%. And the value of sup(F_{phc})-inf(F_{phc}) rapidly stabilizes around 4.31, as shown in Fig. 11(f). As depicted in Fig. 11(g) and (i), the amplitudes of the PW and CW currents also rise up after the proposed control strategy is activated. The *d*- and *q*-axis components of the 3rd, -3rd, 5th and -5th PW hormonic currents exhibit similar characteristics to those under the sub-synchronous speed, as shown in Fig. 11(h) and (j).

D. Experimental Results Under Load Change

Fig. 12 illustrates the experimental results under load change with and without strategy activation, which are obtained under the same operating condition. The rotor speed is 957 rpm, and the load is initially 74 Ω and changed to 136 Ω at 4.1 s. Figs. 12(a) and (d) illustrate the waveforms of the torque with and without strategy activation under load change. From Fig. 12(c), the peak-to-peak values of the torque with strategy activation are reduced by 48.3% and 48.6% before and after load change compared to those without strategy activation, respectively. Figs. 12(b) and (e) illustrate harmonic analysis of the torque with and without strategy activation. Compared to the non-activated strategy, the contents of the torque 2nd harmonic components with strategy activation decrease by 77.5% and 87.8% before and after load change, while the contents of the torque 4th harmonic components increase by 16.7% and 1%. The similar phenomenon has been explained in Section V-B. Moreover, as shown in Fig. 12(e), with strategy activation, there is no obvious difference in the contents of torque 2nd harmonic and 4th harmonic components before and after load change, which indicates that the control strategy is effective during load variation. Fig. 12(f) illustrates the iterative procedure of the value of sup(F_{phc})-inf(F_{phc}) under load change. The value of sup(F_{phc})-inf(F_{phc}) rapidly changes from 3.8 to 2.4 after load reduction.

E. Experimental Results Under Speed Change

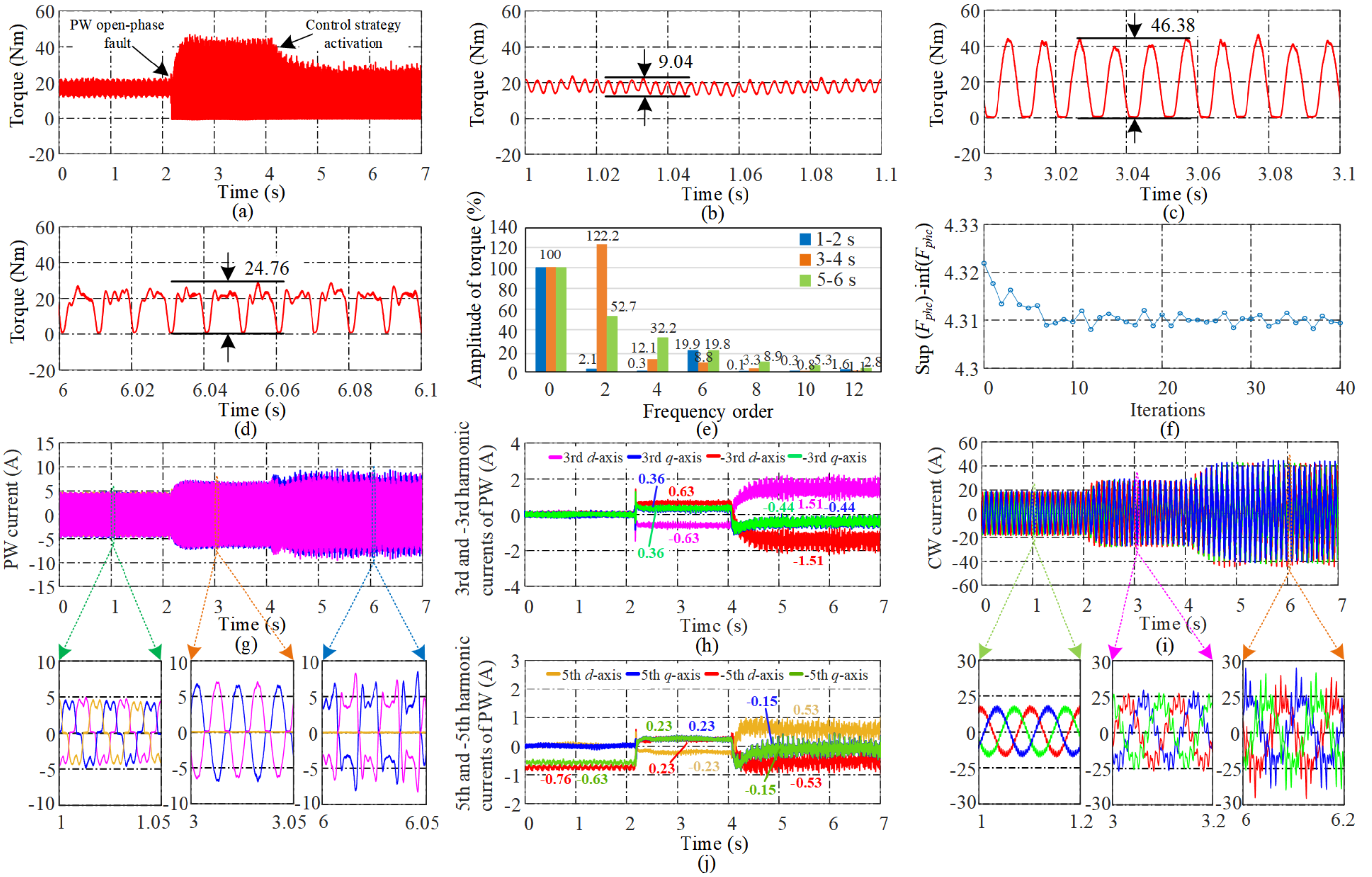

Fig. 11. The experimental results at super-synchronous speed. (a) Torque. (b) Detailed view of the torque from 1 to 1.1 s. (c) Detailed view of the torque from 3 to 3.1 s. (d) Detailed view of the torque from 6 to 6.1 s. (e) Harmonic analysis of the torque. (f) Value of sup(F_{phc})-inf(F_{phc}). (g) PW current. (h) *D*- and *q*-axis components of the PW 3rd and -3rd harmonic currents. (i) CW current. (j) *D*- and *q*-axis components of the PW 5th and -5th harmonic currents.

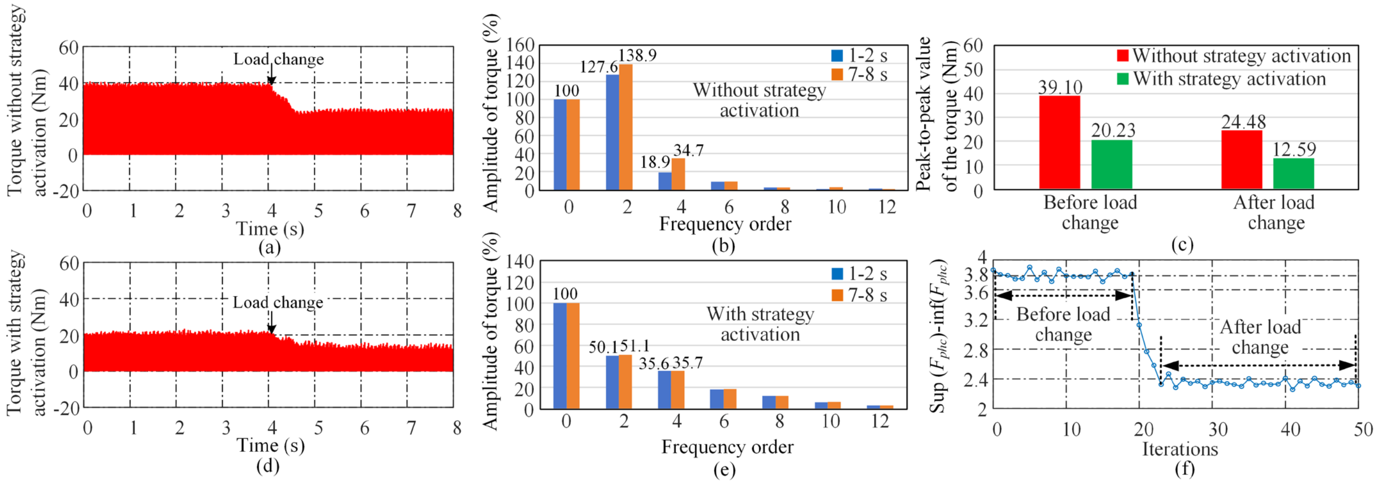

Fig. 12. Experimental results under load change. (a) Torque without strategy activation. (b) Harmonic analysis of the torque without strategy activation. (c) Peak-to-peak values of the torque with and without strategy activation. (d) Torque with strategy activation. (e) Harmonic analysis of the torque with strategy activation. (f) Value of sup(F_{phc})-inf(F_{phc}).

Fig. 13 shows the experimental results under the speed change with and without strategy activation, and the experiments are conducted under the same operating condition with the resistive load of 74 Ω. And the rotor speed is 967 rpm before 3.1 s and it decreases to 853 rpm after 5 s. The waveforms of the torque with and without strategy activation are shown in Figs. 13(a) and (d), respectively. From Fig. 13(c), when the control strategy is enabled, the peak-to-peak values of torque before and after speed change decrease by 48.2% and 47.1%, respectively. As shown in Figs. 13(b) and (e), compared to the non-activated strategy, the contents of the torque 2nd harmonic components with strategy activation decrease by 78.1% and 72.8% before and after speed change, while the contents of the torque 4th harmonic components increase by 14.3% and 20.3%. In addition, when the control strategy is activated, the amplitude of each torque harmonic is without significant variation before and after speed change, which implies that the control strategy is valid during speed variation. The value of sup(F_{phc})-inf(F_{phc}), as shown in Fig. 13(f), promptly rises from 3.6 to 4.5 after speed reduction.

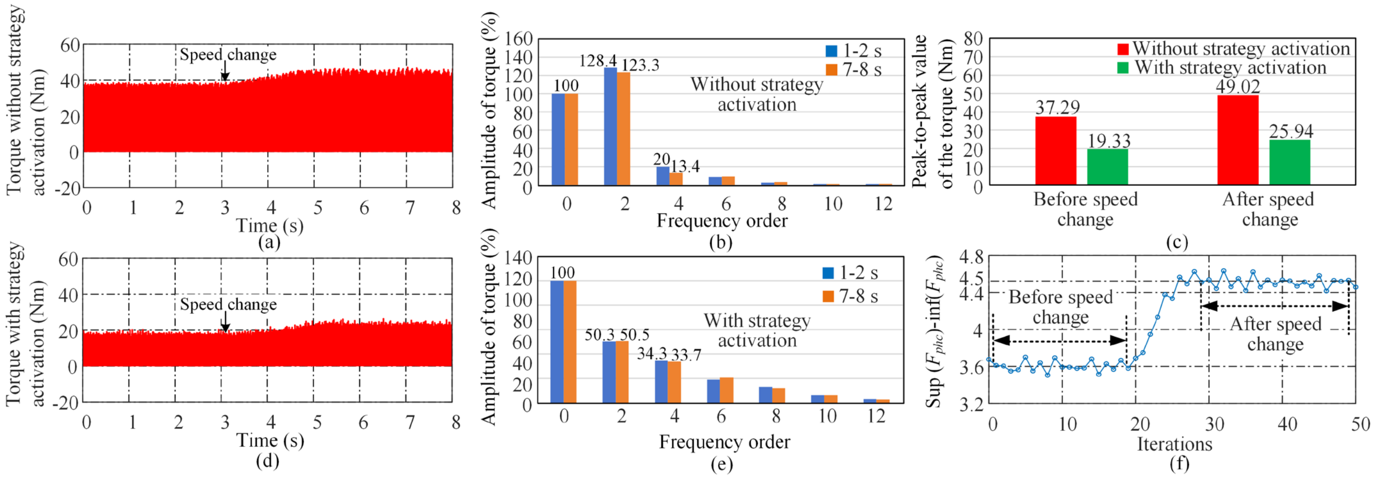

Fig. 13. Experimental results under speed change. (a) Torque without strategy activation. (b) Harmonic analysis of the torque without strategy activation. (c) Peak-to-peak values of the torque with and without strategy activation. (d) Torque with strategy activation. (e) Harmonic analysis of the torque with strategy activation. (f) Value of sup(F_{phc})-inf(F_{phc}).

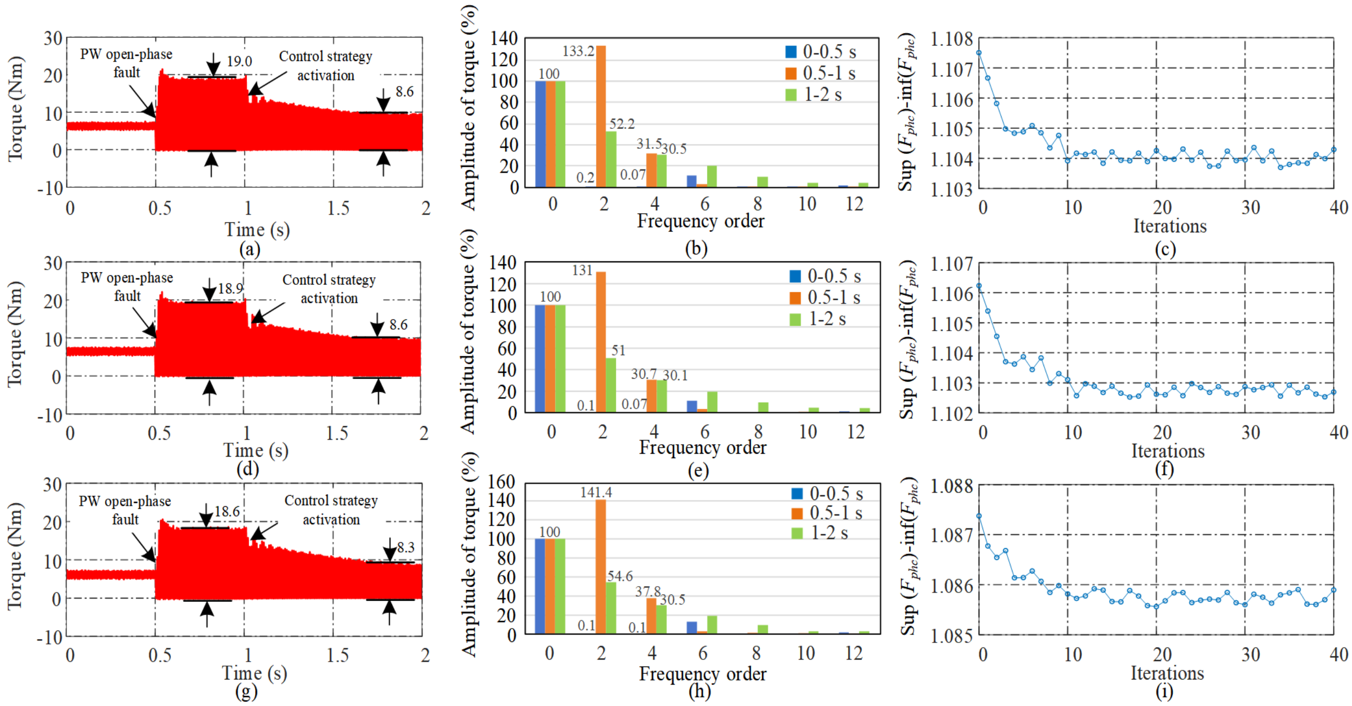

Fig. 14. Simulation results with machine parameters being off. (a) Torque under the original parameters. (b) Harmonic analysis of the torque under the original parameters. (c) Value of sup(F_{phc})-inf(F_{phc}) under the original parameters. (d) Torque under 130% of R_p, R_c and R_r. (e) Harmonic analysis of the torque under 130% of R_p, R_c and R_r. (f) Value of sup(F_{phc})-inf(F_{phc}) under 130% of R_p, R_c and R_r. (g) Torque under 70% of L_p, L_c, L_r, L_{pr} and L_{cr}. (h) Harmonic analysis of the torque under 70% of L_p, L_c, L_r, L_{pr} and L_{cr}. (i) Value of sup(F_{phc})-inf(F_{phc}) under 70% of L_p, L_c, L_r, L_{pr} and L_{cr}.

F. Simulation Results with Machine Parameters Being Off

In order to verify the effectiveness of the proposed strategy under the machine parameters being off, the simulation is conducted with the original machine parameters listed in Table I and the deviated ones.

Fig. 14 illustrates the simulation results under the resistive load of 500 Ω and the super-synchronous speed of 900 rpm.

Besides, the results shown in Fig. 14 are obtained under the original machine parameters, 130% of R_p, R_c and R_r (corresponding to the temperature increasing) and 70% of L_p, L_c, L_r, L_{pr} and L_{cr} (corresponding to the magnetic field saturation), respectively. And, the control parameters, the dc bus voltage and PW frequency in the simulation are the same as those given in the experiments mentioned above. The PW open-phase fault occurs at 0.5 s, and the minimum torque ripple control strategy is activated at 1 s.

From Figs. 14(a), (d) and (g), the peak-to-peak values of torque decrease by almost the same percentage (54.7%, 54.5% and 55.4%) under the three sets of machine parameters mentioned above, after the strategy is activated. Besides, as shown in Figs. 14(b), (e) and (h), the contents of the torque 2nd harmonic components are reduced by 81%, 80% and 86.8% with the strategy activation compared to those without the strategy activation, respectively. Figs. 14(c), (f) and (i) demonstrates the value of sup(F_{phc})-inf(F_{phc}) under the three sets of machine parameters, which rapidly stabilizes around 1.104, 1.103 and 1.086, respectively.

As can be observed form Fig. 14, the proposed strategy still works well with the same control parameters under significant machine parameters variation.

VI. CONCLUSION

In this article, a minimum torque ripple control strategy without external devices is proposed for the BDFIG-DC system under the PW open-phase fault to enhance the system reliability. Initially, the torque harmonic components under the PW open-phase fault are analyzed. Then, the PW harmonic flux with a relatively small proportion is ignored and the PLL is adopted to establish a concise torque expression under the PW open-phase fault. For the main proportion of the simplified torque expression, the solution of the minimum torque ripple under the PW open-phase fault can be converted to minimize the fluctuation of the constructed PW harmonic currents objective function. In order to cope with the nonlinear and non-analytical issues in the solution process for optimal PW harmonic currents, the Newton's gradient descent method is employed for the numerical iterative solution. Moreover, the PW harmonic current control module is designed to further enhance the robustness of the control system. Finally, the effectiveness of the proposed minimum torque ripple control strategy is fully proven by the comprehensive experimental results, which indicates that the torque peak-to-peak value can be reduced by 46.6% at least under the PW open-phase fault.

VII. APPENDIX

$$\begin{bmatrix} i_{pd(2v-1)}^{(2v-1)} \\ i_{pq(2v-1)}^{(2v-1)} \\ i_{p0(2v-1)}^{(2v-1)} \end{bmatrix} = \begin{bmatrix} \cos[(2v-1)\hat{\theta}_p] & \cos[(2v-1)\hat{\theta}_p - \frac{2}{3}\pi] & \cos[(2v-1)\hat{\theta}_p + \frac{2}{3}\pi] \\ -\sin[(2v-1)\hat{\theta}_p] & -\sin[(2v-1)\hat{\theta}_p - \frac{2}{3}\pi] & -\sin[(2v-1)\hat{\theta}_p + \frac{2}{3}\pi] \\ \frac{1}{2} & \frac{1}{2} & \frac{1}{2} \end{bmatrix} \begin{bmatrix} i_{pa(2v-1)} \\ i_{pb(2v-1)} \\ i_{pc(2v-1)} \end{bmatrix} \tag{A1}$$

$$\begin{bmatrix} i_{pd-(2v-1)}^{-(2v-1)} \\ i_{pq-(2v-1)}^{-(2v-1)} \\ i_{p0-(2v-1)}^{-(2v-1)} \end{bmatrix} = \begin{bmatrix} \cos[-(2v-1)\hat{\theta}_p] & \cos[-(2v-1)\hat{\theta}_p - \frac{2}{3}\pi] & \cos[-(2v-1)\hat{\theta}_p + \frac{2}{3}\pi] \\ -\sin[-(2v-1)\hat{\theta}_p] & -\sin[-(2v-1)\hat{\theta}_p - \frac{2}{3}\pi] & -\sin[-(2v-1)\hat{\theta}_p + \frac{2}{3}\pi] \\ \frac{1}{2} & \frac{1}{2} & \frac{1}{2} \end{bmatrix} \begin{bmatrix} i_{pa-(2v-1)} \\ i_{pb-(2v-1)} \\ i_{pc-(2v-1)} \end{bmatrix}. \tag{A2}$$

REFERENCES

[1] X. Li, W. Jiang, J. Wang, P. Wang, and X. Wu, "An autonomous control scheme of global smooth transitions for bidirectional dc-dc converter in dc microgrid," *IEEE Trans. Energy Convers.*, vol. 36, no. 2, pp. 950–960, Jun. 2021.

[2] T. Dragicevic, X. Lu, J. Vasquez, and J. Guerrero, "DC microgrids–part I: a review of control strategies and stabilization techniques," *IEEE Trans. Power Electron.*, vol. 31, no. 7, pp. 4876-4891, Jul. 2016.

[3] T. Dragicevic, X. Lu, J. C. Vasquez, and J. M. Guerrero, "DC microgrids—Part II: a review of power architectures, applications, and standardization issues," *IEEE Trans. Power Electron.*, vol. 31, no. 5, pp. 3528–3549, May 2016.

[4] Y. Lin, Y. Liu, W. Xu, M. G. Hussien, and E. M. Rashad, "An improved speed observer based on super-twisting algorithm for standalone brushless doubly-fed induction generator-dc system," in *Proc. IEEE 25th Int. Conf. Elect. Machines Syst.*, 2022, pp. 1–6.

[5] Y. Liu *et al.*, "Improved efficiency optimization control for brushless doubly fed induction generator–dc system by regulating stator frequency," *IEEE Trans. Power Electron.*, vol. 38, no. 3, pp. 3624–3639, Mar. 2023.

[6] C. Rahmann, V. Vittal, J. Ascui, and J. Haas, “Mitigation control against partial shading effects in large-scale PV power plants,” *IEEE Trans. Sustain. Energy*, vol. 7, no. 1, pp. 173–180, Jan. 2016.

[7] C. N. Papadimitriou, V. A. Kleftakis, and N. D. Hatziargyriou, “A novel method for islanding detection in dc networks,” *IEEE Trans. Sustain. Energy*, vol. 8, no. 1, pp. 441–448, Jan. 2017.

[8] X. Fan, J. Shu, and B. Zhang, “Coordinated control of dc grid and offshore wind farms to improve rotor-angle stability,” *IEEE Trans. Power Syst.*, vol. 33, no. 4, pp. 4625–4633, Jul. 2018.

[9] B. A. Welchko, T. M. Jahns, and S. Hiti, “IPM synchronous machine drive response to a single-phase open circuit fault,” *IEEE Trans. Power Electron.*, vol. 17, no. 5, pp. 764–771, Sep. 2002.

[10] A. Hajary, R. Kianinezhad, S. G. Seifossadat, S. S. Mortazavi, and A. Saffarian, “Detection and localization of open-phase fault in three-phase induction motor drives using second order rotational park transformation,” *IEEE Trans. Power Electron.*, vol. 34, no. 11, pp. 11241–11252, Nov. 2019.

[11] Z. Song, Y. Jia, and C. Liu, “Open-phase fault-tolerant control strategy for dual three-phase permanent magnet synchronous machines without controller reconfiguration and fault detection,” *IEEE Trans. Power Electron.*, vol. 38, no. 1, pp. 789–802, Jan. 2023.

[12] Y. Liu and W. Xu, *Advances in Control Technologies for Brushless Doubly-fed Induction Generators*. Singapore: Springer Nature, 2022.

[13] Y. Jiang, M. Cheng, and P. Han, "Analysis and dynamic control of a dual-stator BDFIG-DC system supplying dc grid with minimized torque ripple through harmonic component current injection," *IEEE Trans Power Electron*, vol. 34, no. 6, pp. 5388-5399, Jun. 2019.

[14] M. Zhang, Y. Liu, W. Xu, and S. Huang, “Torque ripple suppression for standalone brushless doubly-fed induction generator-dc system based on power winding harmonic current control,” *IEEE Trans. Ind. Electron.*, vol. 70, no. 9, pp. 8746–8756, Sep. 2023.

[15] M. Zhang, Y. Liu, and W. Xu, “Improved torque ripple suppression strategy for brushless doubly fed induction generator-dc system considering winding harmonic loss,” *IEEE Trans. Power Electron.*, vol. 39, no. 1, pp. 1209–1220, Jan. 2024.

[16] N. Bianchi, S. Bolognani, M. Zigliotto, and M. Zordan, “Innovative remedial strategies for inverter faults in IPM synchronous motor drives,” *IEEE Trans. Energy Conversion*, vol. 18, no. 2, pp. 306–314, Jun. 2003.

[17] B. Touaiti, M. Moujahed, H. Ben Azza, and M. Jemli, “Fault-tolerant VSI for stand-alone DFIG feeding an isolated dc load,” *Int. J. Electron*, vol. 105, no. 10, pp. 1769–1784, Oct. 2018.

[18] M. Naidu, S. Gopalakrishnan, and T. W. Nehl, “Fault-tolerant permanent magnet motor drive topologies for automotive X-by-wire systems,” *IEEE Trans. Ind. Appl.*, vol. 46, no. 2, pp. 841–848, Mar./Apr. 2010.

[19] K. Ni, Y. Hu, G. Chen, C. Gan, and X. Li, “Fault-tolerant operation of DFIG-WT with four-switch three-phase grid-side converter by using simplified SVPWM technique and compensation schemes,” *IEEE Trans. Ind. Appl.*, vol. 55, no. 1, pp. 659–669, Jan. 2019.

[20] H. Xu, W. Huang, F. Bu, H. Liu, and X. Lin, “Control of five-phase dual stator-winding induction generator with an open phase,” *IEEE Trans. Ind. Electron.*, vol. 66, no. 1, pp. 696–706, Jan. 2019.

[21] W.-S. Im, J.-M. Kim, D.-C. Lee, and K.-B. Lee, “Diagnosis and fault-tolerant control of three-phase ac-dc PWM converter systems,” *IEEE Trans. Ind. Appl.*, vol. 49, no. 4, pp. 1539–1547, Jul. 2013.

[22] C. M. Hackl, U. Pecha, and K. Schechner, “Modeling and control of permanent-magnet synchronous generators under open-switch converter faults,” *IEEE Trans. Power Electron.*, vol. 34, no. 3, pp. 2966–2979, Mar. 2019.

[23] J.-S. Lee and K.-B. Lee, “Open-switch fault tolerance control for a three-level NPC/T-type rectifier in wind turbine systems,” *IEEE Trans. Ind. Electron.*, vol. 62, no. 2, pp. 1012–1021, Feb. 2015.

[24] J.-S. Lee and K.-B. Lee, “An open-switch fault detection method and tolerance controls based on SVM in a grid-connected T-type rectifier with unity power factor,” *IEEE Trans. Ind. Electron.*, vol. 61, no. 12, pp. 7092–7104, Dec. 2014.

[25] Y. Liu, M. Zhang, W. Xu, E. M. Rashad, and M. G. Hussien, “Optimized torque ripple suppression method for standalone brushless doubly fed induction generator with special loads,” *IEEE Trans. Power Electron.*, vol. 37, no. 9, pp. 10981–10993, Sep. 2022.

[26] B. K. Bose, *Modern Power Electronics and AC Drives*. Englewood Cliffs, NJ, USA: Prentice-Hall, 2002.

[27] J. Poza, E. Oyarbide, D. Roye, and M. Rodriguez, “Unified reference frame dq model of the brushless doubly fed machine,” *Proc. Inst. Elect. Eng.-Elect. Power Appl.*, vol. 153, no. 5, pp. 726–734, Sep. 2006.

[28] P. Rodriguez, A. Luna, I. Candela, R. Mujal, R. Teodorescu, and F. Blaabjerg, “Multiresonant frequency-locked loop for grid synchronization of power converters under distorted grid conditions,” *IEEE Trans. Ind. Electron.*, vol. 58, no. 1, pp. 127–138, Jan. 2011.

[29] M. Cheng, Y. Jiang, P. Han, and Q. Wang, “Unbalanced and low-order harmonic voltage mitigation of stand-alone dual-stator brushless doubly fed induction wind generator,” *IEEE Trans. Ind. Electron.*, vol. 65, no. 11, pp. 9135–9146, Nov. 2018.